Pharm Res (2011) 28:1995–2007
DOI 10.1007/s11095-011-0426-5

RESEARCH PAPER

How Stealthy are PEG-PLA Nanoparticles? An NIR *In Vivo* Study Combined with Detailed Size Measurements

Andreas Schädlich • Cornelia Rose • Judith Kuntsche • Henrike Caysa • Thomas Mueller • Achim Göpferich • Karsten Mäder

Received: 18 January 2011 / Accepted: 8 March 2011 / Published online: 27 April 2011

ABSTRACT

Purpose Detailed *in vivo* and *ex vivo* analysis of nanoparticle distribution, accumulation and elimination processes were combined with comprehensive particle size characterizations.

Methods The *in vivo* fate of near infrared (NIR) nanoparticles in nude mice was carried out using the Maestro™ *in vivo* fluorescence imaging system. Asymmetrical field flow field fractionation (AF4) coupled with multi-angle laser light scattering (MALLS), photon correlation spectroscopy (PCS) and transmission electron microscopy (TEM) were employed for detailed *in vitro* characterization.

Results PEG-PLA block polymers were synthesized and used for the production of defined, stable, nontoxic nanoparticles. Nanoparticle analysis revealed narrow size distribution; AF4/MALLS permitted further accurate size evaluation. Multispectral fluorescence imaging made it possible to follow the *in vivo* fate non-invasively even in deep tissues over several days. Detailed fluorescence *ex vivo* imaging studies were performed and allowed to establish a calculation method to compare nanoparticle batches with varying fluorescence intensities.

Conclusion We combined narrow-size distributed nanoparticle batches with detailed *in vitro* characterization and the understanding of their *in vivo* fate using fluorescence imaging, confirming the wide possibilities of the non-invasive technique and presenting the basis to evaluate future size-dependent passive tumor accumulation studies.

KEY WORDS AF4 · fluorescence imaging · *in vivo* imaging · nanoparticle · PEG-PLA

ABBREVIATIONS

AF4	asymmetrical field flow field fractionation
CHO	Chinese hamster ovary
DiR	1,1′-dioctadecyl-3,3,3′,3′-tetramethylindotricarbocyanine iodide
EMEM	Eagle's minimum essential medium
EPR	enhanced permeability and retention
FBS	fetal bovine serum
MALLS	multi-angle laser light scattering
MTT	3-(4,5-Dimethylthiazol-2-yl)-2,5-diphenyltetrazolium bromide
NIR	near infrared
NR	nile red
PBS	phosphate-buffered saline
PCS	photon correlation spectroscopy
PDI	polydispersity indices
QD	quantum dots
RES	reticuloendothelial system

A. Schädlich · J. Kuntsche · K. Mäder (✉)
Department of Pharmaceutical Technology and Biopharmaceutics
Martin Luther University Halle-Wittenberg
Wolfgang-Langenbeck-Str. 4
06120 Halle (Saale), Germany
e-mail: Maeder@pharmazie.uni-halle.de
URL: http://www.pharmtech.uni-halle.de/

C. Rose · A. Göpferich
Department of Pharmaceutical Technology University of Regensburg
Universitätsstraße 31 93053 Regensburg, Germany

H. Caysa · T. Mueller
Department of Internal Medicine IV, Oncology/Hematology
Martin Luther University Halle-Wittenberg
06120 Halle (Saale), Germany

ROI region of interest
TEM transmission electron microscopy

INTRODUCTION

The development of biodegradable nanoparticles as drug delivery vehicles for therapeutic agents is one of the main promises for future cancer therapies. The major aim is to produce nanoparticles which preferentially accumulate at the tumor site. Loaded with anticancer drugs, they can improve cancer therapy and simultaneously reduce the harmful nonspecific side effects of chemotherapeutics (1). In addition, nanoparticles loaded with contrast agents may provide very efficient cancer diagnostics by *in vivo* imaging. Two main tumor targeting strategies have generally been explored: First, active targeting by conjugating nanocarriers with molecules that can bind to tumor-specific antigens or receptors on the cancer cells (2), and second, the more commonly used passive targeting strategy. The first marketed products were introduced more than 10 years ago as liposomes or polymer-protein conjugates (2). The passive accumulation of nanoparticles is based on the enhanced permeability and retention (EPR) effect of tumor tissues (3). Several studies have shown that particle size plays a key role in accumulation effectiveness. Experiments using liposomes have demonstrated that the upper size limit for extravasations into tumors is about 400 nm (4). Others showed that smaller particles with sizes below 200 nm are even more effective (5–7). However, particles smaller than 20–30 nm are eliminated faster by renal excretion (8). It was also noticed that liposomes, which are smaller than 70 nm, were more rapidly cleared from the circulation than larger (between 70 and 300 nm) ones (9, 10). Therefore, the optimal size of nanoparticles for cancer treatment should be between about 70 and 200 nm (11). Accurate knowledge of the particle size, size distributions, and particle morphology is a key requirement for *in vivo* applications of newly developed nanoparticles, although this is often neglected. Gaumet *et. al*, for example, criticized that conclusions of size-dependent studies of nanoparticle biodistribution are often done without providing accurate particle size data (12). High polydispersity indices (PDI) varying between 0.2 and 0.5 may result in particle overlapping and hamper accurate size-dependent interpretation of the *in vivo* results (12). Besides the size, surface properties of nanoparticles also play an important role for their *in vivo* fate. It is well established that hydrophilic surfaces, which can be achieved, for example, by polymer modification with polyethylene glycol (PEG), reduce opsonisation and thus uptake by the mononuclear phagocytic system (MPS) (11,13). Furthermore, such PEG shells provide sterical stabilization of the particles in aqueous systems (14).

In this study, detailed non-invasive *in vivo* fluorescence imaging experiments were combined with fundamental *in vitro* tests to allow meaningful data interpretation and to gain information about the *in vivo* fate of PEG-PLA nanoparticles. Multispectral *in vivo* fluorescence imaging has already been used for fluorescence tissue imaging with nanocarriers like quantum dots (QD) (15–17). Using NIR QD, it could be shown that fluorescence imaging is possible even in deep tissues (18). Nevertheless, QD are criticized due to the high production costs and the potential *in vivo* toxicity depending on their surface properties (19). The incorporation of the very lipophilic NIR carbocyanine dye DiR into PEG-PLA nanoparticles combined the advantages of NIR light with low toxicity risks for the animals. Fluorescence imaging thus allowed the study of distribution, accumulation and elimination processes of the nanoparticles over several days non-invasively. The distribution of the nanoparticles within the body was comprehensively researched further by additional *ex vivo* experiments. However, fluorescence imaging with different nanoparticle batches (differing in sizes and in polymer composition) may pose constraints, such as varying fluorescence intensities. Due to diversity in dye loading and dye allocation in the particles, direct comparison of the results and particularly quantification in tissues obtained with different nanoparticle batches proved challenging. In this work a new calculation approach is discussed as a basis for future evaluations of size-dependent tumor accumulation studies with different nanoparticle batches. Beyond that, exact size characterization is an important issue, as mentioned above. Particle sizing at the nanoscale is, however, by no means a trivial task. The several methods are based on different measurement principles and the potential existence of various particle species as well as heterogeneous size distribution. These are only some of the challenges in size determination of colloidal formulations. In the present study, the combination of PCS, AF4 coupled with MALLS and TEM provided comprehensive information about the size and morphology of the nanoparticles as a basis for drawing meaningful conclusions about the *in vivo* fate of nanoparticles.

MATERIALS AND METHODS

Materials

3,6-Dimethyl-1,4-dioxan (D,L-lactide), poly(ethylene glycol) monomethyl ether (mPEG2000; MW = 2000 Da), stannous 2-ethylhexanoate (>95%), phosphotungstic acid (reagent grade), nile red (NR), Eagle's minimum essential medium (EMEM), nutrient mixture HAM's F-12, sodium dodecyl sulphate and sorbitol were obtained from Sigma Aldrich, Germany. PLGA

75:25 (Resomer® 756) was kindly provided by Boehringer Ingelheim AG, Biberach, Germany. Trypsin-EDTA 0.25%, Dulbecco's phosphate-buffered saline (PBS) and 1,1′-dioctadecyl-3,3,3′,3′-tetramethylindotricarbocyanine iodide (DiR) were purchased from Invitrogen, Germany. Sucrose and Triton-X (p.a.) were obtained from Merck KGaA, Germany, and Pluronic® F68 as well as sodium azide from Riedel-de Haën, Seelze, Germany. Polystyrene standard nanoparticles were obtained from Duke Scientific, Paolo Alto, United States (50, 100, 200 nm) and from Beckman Coulter, Germany (300 nm). Fetal bovine serum (FBS) was purchased from Biochrom KG, Berlin, Germany and 3-(4,5-Dimethylthiazol-2-yl)-2,5-diphenyltetrazolium bromide (MTT) from AppliChem GmbH, Darmstadt, Germany. All other substances and solvents were used as received.

Synthesis and Characterization of PEG-PLA Polymers

Biodegradable diblock copolymers PEG_2PLA_{20} and PEG_2-PLA_{40} were synthesized following a previously established method (20). The numbers refer to the molecular weight (kDa) of the respective polymer block. The PLA part was attached to the mPEG part by a ring-opening polymerization of 3,6-dimethyl-1,4-dioxan (D,L-dilactide) using stannous 2-ethyl hexanoate as catalyst. First of all, any trace amounts of water were removed from the educts. Therefore, about 2 g of the $mPEG_{2000}$ were dissolved in 100 mL toluene in a three-neck round-bottom flask and heated; the reflux of 50 mL toluene was distilled off using a water separator. D,L-dilactide and 100 mL toluene (20 g and 40 g, respectively) were added, and again 50 mL of the solvent was distilled off. The final volume of toluene thus did not exceed 100 mL. After addition of 500 µL glacial acid and about 400 mg of the catalyst, the mixture was refluxed for at least 8 h under nitrogen atmosphere. Afterwards, the toluene was removed by distillation with 200 mL methylene chloride and acetone using a rotary evaporator. The obtained viscous polymer was dissolved in acetone and precipitated by dropping into water at 4°C to remove residual catalyst and water-soluble by-products. The precipitate was separated, frozen at −80°C and freeze-dried. Afterwards, the dried polymer was stored under vacuum. The molecular weight of the synthesized polymers was determined by ^{1}H-NMR and GPC (data not shown).

Preparation of Polymer Nanoparticles

Unloaded (batch A, B and C) and loaded (DiR, batch D and NR, batch E) polymeric nanoparticles were prepared by nanoprecipitation (21). Preparation conditions, like polymer concentration, temperature, impact of volumes (polymer phase and external phase) and the influence of stabilizer, were studied preliminarily (22). For nanoparticle preparation, the respective polymer (2.5, 5 or 10 mg) and—if applicable—the fluorescence dye were dissolved in 5 mL acetone (cp. Table I). This organic solution was drop by drop (2 mL per minute) added to 40 mL of an aqueous poloxamer solution (0.25% w/v Pluronic® F68) to facilitate immediate nanoparticle formation. After evaporation of the organic solvent overnight at room temperature, the particles were collected by centrifugation (12,500 g; 30 min; 10°C) using an Avanti JE high-speed centrifuge (Beckman Coulter, Germany) and washed with filtrated (<1 µm) water. The particles were resuspended in a solution of either 5 or 10% (w/v) sucrose. Subsequently, particles were frozen at −80°C for 24 h and freeze-dried at 15°C and 0.120 mbar over at least 2 days using a lab-scale freeze-dryer (Martin Christ Gefriertrocknungsanlagen, Osterode am Harz, Germany). Dried samples were sealed and stored in a desiccator at room temperature under light protection. For stability evaluation, samples of batch A, B and C were redispersed in bi-distilled water preserved with

Table I Nanoparticle Compositions and Particle Sizes of Different Nanoparticle Batches Measured Directly After Redispersion

Batch Polymer [a]	A PLGA	B PEG_2PLA_{20}	C PEG_2PLA_{40}	D PEG_2PLA_{40}–DiR	E PEG_2PLA_{40}–NR
Dye loading [b]	–	–	–	0.5%	0.6%
Polymer concentration [c]	1.0%	1.0%	1.0%	2.0%	1.0%
PCS - z-average in nm (PDI)	339 (0.52) 209 (0.15)[d]	113 (0.09)	104 (0.08)	166 (0.13)	103 (0.08)
TEM (nm)	128 ± 13	82 ± 15	–	–	–
MALLS D10 (nm)	127 ± 10.4	66 ± 0.9	62 ± 0.1	48 ± 9.8	59 ± 0.4
MALLS D50 (nm)	222 ± 9.0	95 ± 0.2	86 ± 1.0	99 ± 4.0	81 ± 0.3
MALLS D90 (nm)	403 ± 29.8	141 ± 0.6	132 ± 0.4	230 ± 3.3	121 ± 0.2

[a] The numbers 2 and 20 refer to the molar mass of the polymer block (kDa)

[b] Dye loading in percent related to the polymer amount

[c] Polymer concentration in percent related to the organic solvent

[d] Sample was filtered (pore size 0.8 µm) prior measurements

0.02% (w/v) sodium azide and stored in the fridge (5°C) for 3 months.

Particle Size Characterization of Nanoparticles

Photon Correlation Spectroscopy (PCS)

Dynamic light scattering was measured at 25°C in the backscattering mode (173°) with a High Performance Particle Sizer (HPPS) from Malvern Instruments (Malvern, Herrenberg, Germany). Samples were diluted with purified, filtered (0.2 μm) water (nanoparticle concentration was about 0.1 mg/mL) and measured 4 times with 12–16 runs over 10 s each at fixed measurement position in the middle of the cuvette. Due to macroscopic inhomogeneities, PLGA suspensions were filtrated (pore size 0.8 μm, PALL medical, Dreieich, Germany) and measured once again. Z-average diameters and PDI were determined by the instruments cumulant analysis software (version 4.20). Results are given as average with standard deviation of the 4 measurements ($n=4$).

Asymmetrical Flow Field-Flow Fractionation (AF4)

Samples were analyzed as described earlier (23). In brief, the fractionation system (Eclipse AF4, Wyatt, Dernbach, Germany) was coupled with a multi-angle laser light scattering (MALLS) detector (DAWN EOS, Wyatt). The trapezoidal channel (length 265 mm, largest width 21 mm, height 350 μm) was equipped with a membrane of regenerated cellulose or polyethersulfone (MWCO 5 kDa, Microdyn-Nadir, Wiesbaden, Germany). Bi-distilled water preserved with 0.02% sodium azide and filtered through 0.1 μm was used as carrier liquid. One hundred μL dispersion (nanoparticle concentration about 1 mg/mL) was injected during focusing (focus flow 2 mL/min), and samples were eluted with a constant detector flow of 1 mL/min and decreasing cross flow. Initially, a high cross flow gradient (cross flow decreasing from 2 to 0.5 mL/min within 5 min) was applied to assure baseline separation of the nanoparticles from the void peak followed by a decreasing cross flow (0.5–0 mL/min within 35 min) to separate the nanoparticles. Size evaluations were done by the Astra software 4.90 (Wyatt) using the particle mode and assuming compact spheres (23). Mass weighted size distributions and the characteristic diameters (D10, D50, and D90) were calculated using the binning method (23). Similarly as in PCS measurements, the dispersion of PLGA nanoparticles was filtered (pore size 0.8 μm) prior to the measurements. The separation accuracy of the A4F/MALLS system was checked by using a mixture of 50, 100, 200 and 300 nm polystyrene standard nanoparticles as described earlier (23). All samples were measured in triplicate, and results are given as average with standard deviation ($n=3$).

Transmission Electron Microscopy (TEM)

About 10 μL of diluted aqueous nanoparticle dispersions were placed on 3.05 mm formvar/carbon-coated copper grids (300 mesh) and negatively stained with phosphotungstic acid (2% in water) for 30 s. Samples were subsequently dried under vacuum and viewed in a Zeiss EM C/CR (Carl Zeiss AG, Germany) at 60 kV operating voltage. Particle size was estimated by manually measuring the diameter of 100 randomly chosen particles for each sample. The mean size was determined for each sample in triplicate ($n=3$).

In Vitro Cytotoxicity Assay

Biocompatibility was tested with hamster endothelia (chinese hamster ovary (CHO)) cells and mouse fibroblasts (L929). They were cultured in HAMs F12 and EMEM, respectively, each supplemented with 10% FBS at standard cell culture conditions (37°C; 95% relative humidity and 5% CO_2). Evaluation was done using the well-established MTT assay (24). Twenty four h after seeding the cells in 96 well-plates, media were removed and 0.01, 0.1 and 1 mg/mL of PLGA or PEG_2PLA_{20} nanoparticles, redispersed in cell culture medium, were added. After 4 h of incubation at standard conditions, the cell culture medium was removed, and cells were washed once with PBS (pH=7.2). Afterwards, 200 μL of a MTT in PBS solution was added to each well (final concentration of 0.4 mg/mL), and cultures were again incubated for 4 h under the same conditions. Thereafter, the supernatant was carefully aspirated, and a solution of sodium dodecyl sulphate (10% in PBS) was added for cell lysis. For the dissolution of the precipitated formazan crystals, the well-plates were stored over 24 h at room temperature under exclusion of light. Subsequently, quantitative formazan concentration was determined by measuring the optical density at 550 nm with a background correction at 630 nm using an automatic microplate reader (TiterTek Plus, Germany). The water-soluble MTT is only converted into an insoluble formazan dye by the mitochondrial dehydrogenase by living cells (25). Cytotoxicity is expressed as cell viability of the treated cells relative to the untreated ones (negative control). A solution of Triton X 0.5% in PBS was used as a positive control; untreated cells with medium served as a negative control, and blank values were obtained from cell-free medium.

In Vivo Imaging and Analysis

Distribution, accumulation and elimination processes were studied by measuring the fluorescence signal of the respective dye which was incorporated into the nanoparticles. All procedures of the *in vivo* experiments complied with the standards for use of animal subjects as stated in the

guideline from the animal care and use committee of Saxony Anhalt. All *in vivo* studies were performed in nude, female and male mice (Crl:SKH1-Hr^{hr}, 25–30 g) from Charles River Lab, which have humoral and cellular immunity comparable to C57B1/6 mice (26). All mice were housed under controlled conditions (12 h light/dark schedule, 24°C).

An aliquot (2.0, 4.0, 6.0 and 6.5 mg polymer, 5% sucrose) of the freeze-dried fluorescent nanoparticles was redispersed in 1 ml of purified water and isotonised with sorbitol. Sixty µL of each sample were then slowly injected into the tail vein of non-narcotized mice. During the imaging procedure, a mixture of isofluorane/oxygen was used as anaesthesia gas with an initial flow of 4% isofluorane (3.0 L/min oxygen) and a steady-state flow of 1.8% isofluorane (1.5 L/min oxygen). All mice were placed under same conditions (stage height, mouse position, objective adjustment) on a 35°C temperature-controlled heating plate to protect them for cooling out.

All *in vivo* fluorescence imaging measurements were carried out using the Maestro™ *in vivo* fluorescence imaging system (Cambridge Research & Instrumentation, Woburn, United States) and the Maestro™ software (version 2.10) (27). A Cermax®-type 300 Watt Xenon lamp with 5600 K, a NIR excitation filter (710–760 nm) and an 800 nm long-pass emission filter were used to detect DiR. The software acquired multispectral image cubes in 10 nm steps in the spectral range between 780 and 950 nm. The exposure time was automatically set to optimum values by the software (autoexpose function). An *in vitro* reference spectrum was obtained from the aqueous dispersion of DiR-loaded nanoparticles prior to injection, and the *in vivo* reference DiR spectrum was generated 45 min after the injection by the signal from the nanoparticles accumulated in the liver. This signal was corrected by the manual compute function using the auto-fluorescence signal of an untreated mouse, which was measured under the same conditions. This auto-fluorescence signal was also set as background for all further data evaluations. This way, the received emission information could be divided (unmixed) into parts allocated to auto-fluorescence of the body and those caused by the nanoparticles (28,29). Using both spectra, grayscale images were generated from each of the respective emission spectra. These pictures were then used for the calculation of intensity weighted images using an incremental jet color profile. The software's 'compare images' function allows comparison of images taken under different conditions (*e.g.* exposure times). Therefore, all grayscale DiR images were correlated to the respective exposure times. Pixels with maximum intensities are set to dark red, and pixels with zero fluorescence to black with a gradation from red to orange, yellow, light and dark blue in between. Detection of NR was carried out with the green filter set (excitation filter: 503–555 nm, emission filter: 580 nm long-pass, acquisition setting: 550–800 nm) in 2 nm steps. Fluorescent imaging files were acquired during the first hour after injection. All other parameters accorded to the DiR measurements.

Ex Vivo Imaging and Analysis

For *ex vivo* analysis, the mice were sacrificed using carbon dioxide 24 h after injecting the nanoparticles. Excised organs were imaged with the Maestro™ *in vivo* imaging system. To ensure reproducible conditions like the arrangement of the organs, positioning in the Maestro™, incident angle of the light, *etc*., the organs or respective organ parts (intestine and liver in the size of the hole) were placed into a 24-holes well-plate. The imaging procedure accorded with the *in vivo* measurements. To detect potential minor accumulation in different organs, exposure times above the autoexposed values were used. Therefore, the liver was masked with a black plastic plate to inhibit an overexposure. For further calculation and evaluation, a region of interest (ROI) in the size of the holes of the well-plate was generated, and the corresponding exposure-time weighted total and maximum fluorescence signals were calculated. To exclude the influence of different dye amounts due to varying nanoparticle concentration, the *ex vivo* total intensity value was divided through the maximum intensity of the *in vitro* emission spectra of the nanoparticles. These *in vitro* spectra were measured prior to injection, all in equal volumes and under the same measurement conditions. Afterwards, all values were normalized to 100% related to the highest fluorescence intensity.

RESULT AND DISCUSSION

Physicochemical Properties

Photon Correlation Spectroscopy (PCS)

PCS allows fast, robust and reproducible measurements of intensity weighed, hydrodynamic mean diameters of particles in the size range between about 5 nm and 2 µm. For the PEG-PLA nanoparticles, hydrodynamic diameters between 104 and 166 nm were measured (Table I and Fig. 1a). PDI values below 0.13 indicate that the nanoparticles are, compared to literature data, rather homogeneous in size (12). A higher polymer amount and the incorporation of DiR increased the particle size to about 60 nm and also slightly the PDI. PLGA nanoparticles were distinctly larger, and the high PDI (0.52) indicates inhomogeneity, which was already macroscopically visible. For the filtered (0.8 µm) dispersion, a z-average of 209 nm and a PDI of 0.15 were measured.

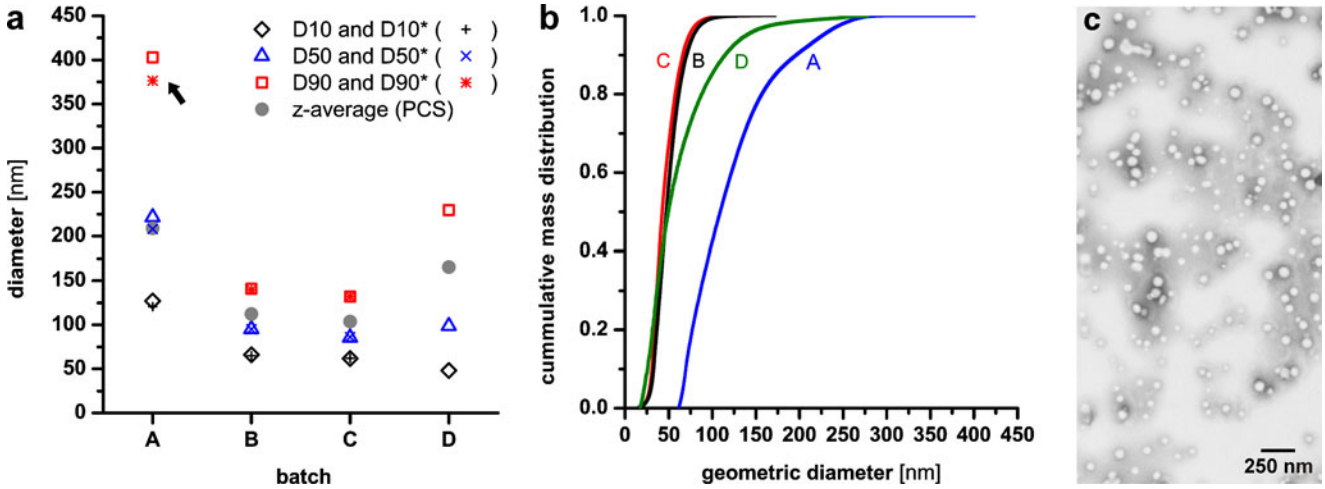

Fig. 1 (**a**) D10, D50 and D90 diameters determined by AF4/MALLS and PCS z-averages measured immediately after redispersion and after 3 months storage (batch **a**, **b** and **c**) at 5°C (marked with *); (**b**) AF4/MALLS cumulative size distributions of freshly redispersed PLGA (**a**), PEG_2PLA_{20} (**b**), PEG_2PLA_{40} (**c**) and PEG_2PLA_{20} – DiR (**d**) nanoparticle suspensions. (**c**) TEM image of batch B nanoparticles.

Transmission Electron Microscopy (TEM)

Visualization of two nanoparticle batches was carried out by TEM of negatively stained samples (Fig. 1c). The dimensions of the nanoparticles are shown in Table I. The sizes were generally smaller than those determined by PCS (30,31) and AF4/MALLS. However, PCS determines the hydrodynamic diameter of particles, which is sensitive to the hydrated PEG chains on the surface of the nanoparticles. In contrast, dried nanoparticles were viewed in TEM, and size calculations are weighted by the number of the particles. Bigger particles are less frequent in the prepared batch than smaller ones. Furthermore, in the light scattering methods larger sample volumes are measured compared to TEM. If there are bigger particles present in the batch, they have a distinct effect to the calculation in PCS, but they will probably not be detected with TEM.

Asymmetrical Flow Field-Flow Fractionation (AF4)

AF4 combined with MALLS allows accurate size evaluation due to sample separation prior size determination (23,32). The characteristic D10, D50 and D90 diameters of the mass-weighted size distributions are shown in Table I and Fig. 1a. PCS z-averages were larger than the median (D50) determined by AF4/MALLS. This is the result of the water binding between the PEG chains on the nanoparticle surfaces as discussed above. This influences the movement of the nanoparticles during the PCS measurements and thereby the detected nanoparticle size. Due to principle of MALLS measurements, which was applied to retrieve geometrical mass weighted particle sizes (RMS radius or radius of gyration) (33), the influence of the water shell is reduced. However, overall the D50 diameters confirm the size trend between the different nanoparticle batches measured in PCS and TEM. The larger difference between the PCS and MALLS results of batch D compared to batch B and C can probably be attributed to the higher sensitivity at both ends of the particle size distribution in the AF4/MALLS, which allows better quantification of smaller and larger particles in the sample. Size distribution was clearly broader in batch D compared to those of batch B and C (Fig. 1b). This is in good agreement with the higher PDI measured with PCS for batch D nanoparticles. The possibility of analyzing the amount of smaller and bigger particles in the dispersion is of great importance for meaningful interpretation of the *in vivo* results. The broad distribution of batch A (PLGA nanoparticles) with D90 values up to 400 nm is also visible in the cumulative size distribution (Fig. 1b), although the sample was filtered before the measurements. Due to this inhomogeneity in size as well as the absence of PEG, which would yield in higher accumulations in the RES (11,13), the PLGA nanoparticles were not studied *in vivo*.

Stability Evaluation

Potential physical instability and polymer degradation during storage in aqueous dispersion were investigated by PCS and AF4/MALLS. The results are shown in Table II. D10, D50 and D90 diameters (AF4/MALLS) are also given in Fig. 1a (marked with *). The size of both PEG-PLA nanoparticle batches stayed constant during storage. This is in accordance with literature data which has shown that such nanoparticles are comparatively stable for several months when stored at 5°C (34,35). They also reported *in vitro* studies at 37°C where they showed polymer and particle degradation within several months. This can be

Table II PCS and AF4/MALLS Particle Sizes of Freshly Dispersed Nanoparticle Batches and After Storage the Diluted Samples for 3 Month at 5°C

Batch	A[b]		B		C	
Polymer[a]	PLGA		PEG_2PLA_{20}		PEG_2PLA_{40}	
	fresh	3 Months	fresh	3 Months	fresh	3 Months
PCS - Z-average in nm (PDI)	209 (0.15)	207 (0.13)	113 (0.09)	113 (0.09)	104 (0.08)	103 (0.05)
MALLS D10 (nm)	127 ± 10.4	121 ± 1.7	66 ± 0.9	65 ± 1.2	62 ± 0.1	62 ± 1.1
MALLS D50 (nm)	222 ± 9.0	208 ± 1.6	95 ± 0.2	95 ± 0.4	86 ± 1.0	86 ± 0.5
MALLS D90 (nm)	403 ± 29.8	377 ± 1.7	143 ± 0.6	140 ± 0.7	132 ± 0.4	132 ± 0.3

[a] The numbers 2 and 20 refer to the molar mass of the polymer block (kDa)

[b] Sample was filtered (pore size 0.8 μm) prior measurements

assigned to possible *in vivo* behaviour and attest comparatively slow particle degradation. The high reproducibility of both PCS and AF4/MALLS results underlines the narrow distribution of the produced nanoparticle batches. The AF4/MALLS size results of (filtered) PLGA nanoparticles showed a slight decrease of the particle size, mainly in the upper size range, which may be an indication of starting polymer degradation (marked with black arrow in Fig. 1a). It has been reported that the rate of PLGA degradation is slightly increased in bigger particles, although this was more pronounced at higher temperatures (35). Overall, results indicate accurate stability of the nanoparticles in the dry state and even in aqueous dispersion, which makes them ideal for further applications.

In Vitro Cytotoxicity Assay

More than 90% of the cells were still viable after treatment with the nanoparticles in a concentration range between 0.01 and 0.1 mg/mL. This is in good accordance with literature data (36). Batch A and B (PLGA and PLA_2-PEG_{20}) nanoparticles might thus be recognized as biocompatible, which was the requirement for further *in vivo* experiments. Good biocompatibility can also be assumed for the PLA_2PEG_{40} nanoparticles due to the similar chemical composition.

In Vivo Imaging

Dialkylcarbocyanine dyes like DiI and DiR are widely used as tracers in living and fixed tissues, cells and *in vivo* imaging experiments (37–39). The emission spectrum of the dyes is very broad, which facilitates exact detection also *in vivo*. Furthermore, they are very stable, have low bleaching properties (38) and remain fluorescent also *in vivo* for up to one year (40). Dyes with fluorescence emission in the NIR region (700–900 nm) are required for detailed *in vivo* characterizations, particularly in deeper tissues (18). Biological tissues have a high photon absorbance of fluorescence emission light in the visible wavelength range (350–700 nm), mainly caused by hemoglobin but also in the upper infrared range (above 900 nm) due to the presence of water (41). In contrast, many tissues are optically transparent in the narrow spectral NIR area. DiR is a favorable dye with a fluorescent emission in the near infrared. Furthermore, as DiR is very lipophilic (42), it is tightly incorporated between the lipophilic PLA chains into the nanoparticles. Representative, measured *in vitro* and extracted *in vivo* emission spectra of DiR and of NR are shown in Fig. 2a. Compared with literature data, the *in vitro* emission maxima of DiR is slightly shifted bathochrom to higher wavelengths. This is caused by the cut-on of the emission filter set of the Maestro™ imaging system. Thus, for DiR the emission maximum was measured *in vitro* at about 818 nm instead of the manufacturer's and published information of about 775 nm (38). However, this effect has no influence on the results and data interpretation, since all spectral analyses were only done with the Maestro™ system and the respective *in vitro* and *in vivo* reference spectra. It is furthermore visible that the DiR emission spectra were similar *in vitro* and *in vivo*, indicating that the penetration of emitted fluorescence light through living tissue has no influence on the spectra profile, thus allowing exact detection of nanoparticles *in vivo*. In contrast, a spectral shift is visible between the *in vitro* and *in vivo* spectra when NR was incorporated into the nanoparticles (batch E, Fig. 2a). This finding can be attributed to the influence of the local polarity on the NR emission maxima. Increasing polarities result in a shift of the emission maxima to higher wavelengths and a decrease of the quantum yield. NR is nearly non-fluorescent in pure aqueous media (43).

Figures 2b and c show the images of a mouse 15 and 40 min after injection of nanoparticles loaded with NR (batch E), indicating that *in vivo* imaging of the nanoparticle distribution is in principal possible also with non-NIR dyes. However, nanoparticle accumulation in liver and spleen could not be detected due to the above-mentioned high

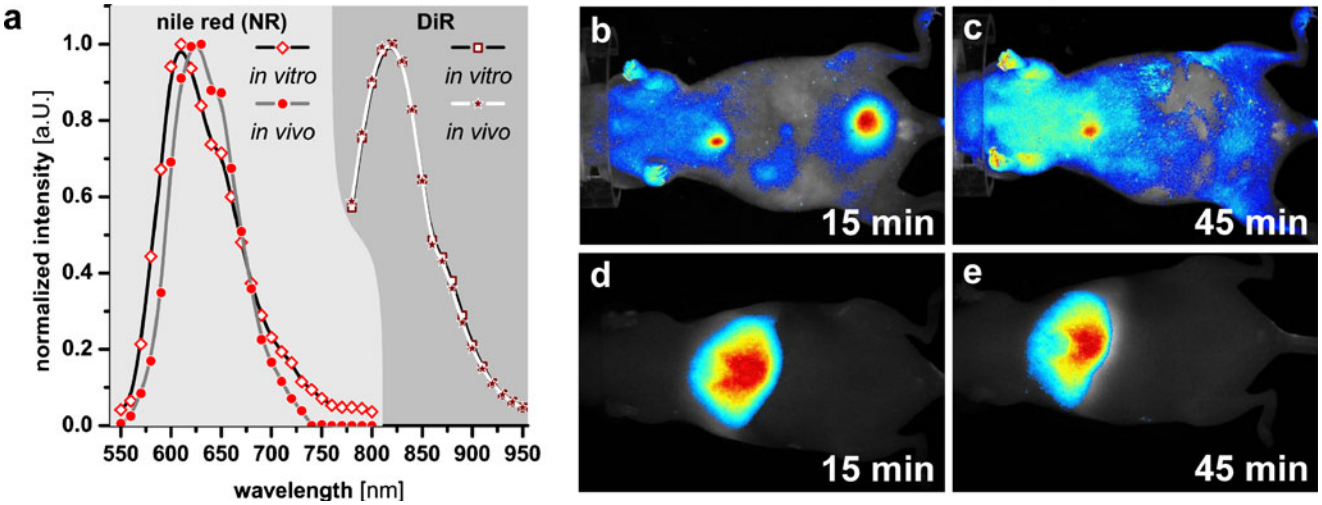

Fig. 2 (**a**) Normalized fluorescence *in vitro* and extracted *in vivo* emission spectra of NR and DiR. The DiR spectra are virtually overlapped. (**b**–**e**) Fluorescence intensity images of two mice 15 (**b**, **d**) and 40 min (**c**, **e**) after injecting NR (**b**, **c**) or rather DiR nanoparticles (**d**, **e**).

photon absorbance of biological tissues. Furthermore, the images agree with *in vitro* NR release studies (44) that showed a fast release of NR from the particles and elimination of the dye through the urine pathway. Due to the low log P value of NR (reported to be 3.8 (45)-5.1 (46)) compared to lipophilic carbocyanine dyes like DiR (log P values between 17.4 (42,47) and 20 (48)), NR is fast released from the particles. Although NR does not fluoresce in water (43), the dye may bind to proteins which are circulating through the blood stream, thus remaining fluorescent (49). The high fluorescence signal in the urine could be caused by binding of NR to smaller proteins, which are normally eliminated by the kidneys via the urine (50).

The very lipophilic properties of the DiR dye prevents a release from the nanoparticles. This is confirmed by other groups who showed that dialkylcarbocynanine is not or is only very slowly released from lipophilic nanocarriers (44, 51). Overall, these results confirm the expectation that for accumulation studies highly lipophilic dyes have to be incorporated to image the fate of nanoparticles in detail. The results after injecting DiR nanoparticles are shown in Fig. 2d and e. An accumulation in the bladder was not detected, as expected.

Distribution Studies

Tests about the *in vivo* fate of nanoparticles as well as the constraints of detection the distribution and accumulation were started by intravenous (i.v.) injection of batch D nanoparticle dispersions. The animals were imaged at various time points (*i.e.*, 5 min after injection, 2 days). The visualized information from the abdomen of a mouse is shown as an inverted grayscale image in Fig. 3. Black is allocated to high DiR emission intensities and white to the background signal. Five min after injection, the blood vessels are clearly visible (Fig. 3b). During the first 6 h these vessels were still detectable, but sharpness and fluorescence

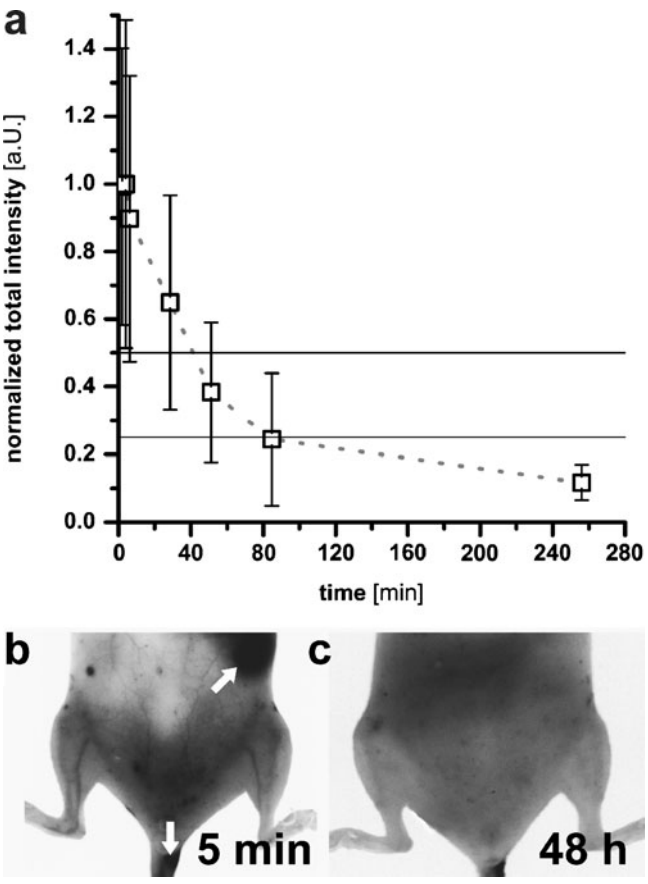

Fig. 3 (**a**) Normalized intensity profile of total signals from the whole body of 5 mice in dependence on time. (**b** and **c**) *In vivo* images of the DiR emission signal from the abdomen of a nude mouse. Arrows mark areas with high fluorescence intensities (spleen and tail due to injection procedure).

intensity decreased slowly. This is in agreement with literature data where the plasma half-life time of about 6 h is given (52). Furthermore, there are two black parts in the image (marked by white arrows). They point to a part of the tail as well as the spleen at the right side of the mouse. A nanoparticle accumulation in the tail can be assigned to the injection procedure, where the tail is slightly fixed by hand to immobilize it. This may result in micro lesions where nanoparticles can pass the vascular wall resulting in a nanoparticle accumulation near the injection site. After 48 h (Fig. 3c), no defined fluorescent areas are identifiable anymore. All nanoparticles are eliminated or at least accumulated in RES body structures.

Due to the resolution of the CCD camera chip, analysis of the blood vessels on their own to calculate blood half-life times was not possible. Instead, the total signal of the whole body from five mice was measured at different time points (Fig. 3a). The calculated values are the sum of all subcutaneous dye signals (from blood vessels, upper parts of liver and spleen). They indicate that 50% of the initially detectable nanoparticles were eliminated after about 45 min and 75% after 95 min. However, as the blood vessels were detectable during the first 6 h, sufficient nanoparticles were still circulating. It is widely known that PLA nanoparticles without surface modification or ones which are only stabilized with poloxamer 188 have a half-life of just a few minutes (52,53). Due to the fact that PEG chains can adopt brush-like structures, they have the ability to reduce phagocytosis *in vivo* (54). The prolonged circulation due to reduced phagocytosis and opsonisation yields a subsequently reduced clearance by the reticuloendothelial system (RES). Consequently, nanoparticles are not eliminated as fast and may accumulate in, *e.g.*, tumor tissues (1,7).

Accumulation Studies

Nanoparticle distribution and accumulation was followed in more detail by imaging the abdominal site of female mice at different time points (Fig. 4a–h). Five min after injection the whole body of the abdomen is homogeneous colored blue with some brighter blue parts in the chest (Fig. 4a), confirming that nanoparticles circulate homogeneously through the body and accumulate in the RES as a part of the immune system where the phagocytic cells are located in reticular connective tissues. After 4 h, the maximal fluorescence is visible in the area of the liver (Fig. 4b). Accumulation of the DiR nanoparticles in the spleen is also visible in the right part of the image (marked by arrow). Accumulation in the spleen could clearly be shown in the jet color images where the color is scaled to the respective image (Fig. 4e and f). Figure 4e shows the homogeneous fluorescent liver and the minor fluorescent spleen (marked by an arrow). During the next few days, nanoparticle accumulation in the RES decreased continuously, but fluorescence was still detectable after five days (Fig. 4d). *In vitro* tests have shown that the polymer degradation strongly depends on temperature and accelerates when temperature is increased, *e.g.* from 5 to >25°C rapidly (34, 35). However, even at 37°C, complete polymer degradation takes still more than one month depending on the dissolution media. Therefore, it can be assumed that the nanoparticles will be also slowly disintegrated *in vivo* and can be detected in the jet color images even five days after injection (Fig. 4h).

Ex Vivo Imaging

Ex vivo studies could provide more detailed information about the nanoparticle accumulation in the different tissues. Mice were sacrificed 24 h after nanoparticle injection, and the respective organs were placed in a 24-holes well-plate (Fig. 4i). Measuring the viscera of an untreated mouse resulted in a black image without any detectable fluorescence signal as shown in Fig. 4j. This control confirms the selectivity in detecting the DiR dye using fluorescence imaging. Figure 4k shows the isolated organs. As expected, high fluorescence intensity was visible in the liver but could also be detected in small parts of the ovaries. No signals were visible in the other organs. However, after masking the liver tissue with a black plastic plate, which allowed higher exposure times, nanoparticle accumulation could also be visualized in the intestine, uterus and spleen (Fig. 4l). The absence of fluorescence in the kidneys indicates that the nanoparticles as well as the dye are not eliminated by urine. This was expected due to the highly lipophilic character of the dye and the size of the nanoparticles. Very lipophilic molecules are often eliminated by bio-conjugation in the liver and excretion via the gall into the intestine (53). Afterwards, they are excreted with the feces. This elimination route was confirmed by the detected fluorescence in the intestine in Fig. 4l.

By implementing a round region of interest (ROI) in the size of the well-plate hole (cp. Fig. 4k) measuring different parameters of each organ became possible, determining total, maximum and average signal intensities, which are related or not related to the respective exposure times. By detailed analysis of this data, quantitative information can be obtained. Maximum and total signal intensities correlated well to the exposure times and were most suitable for further calculations. The maximum intensity values allow the comparison of nanoparticle accumulation in organs differing in size. For example, a high enrichment in a part of a tissue leads to high maximum intensity values within the ROI. The total signal of the same sample, as the sum of all pixels in the ROI, would be, however, only slightly

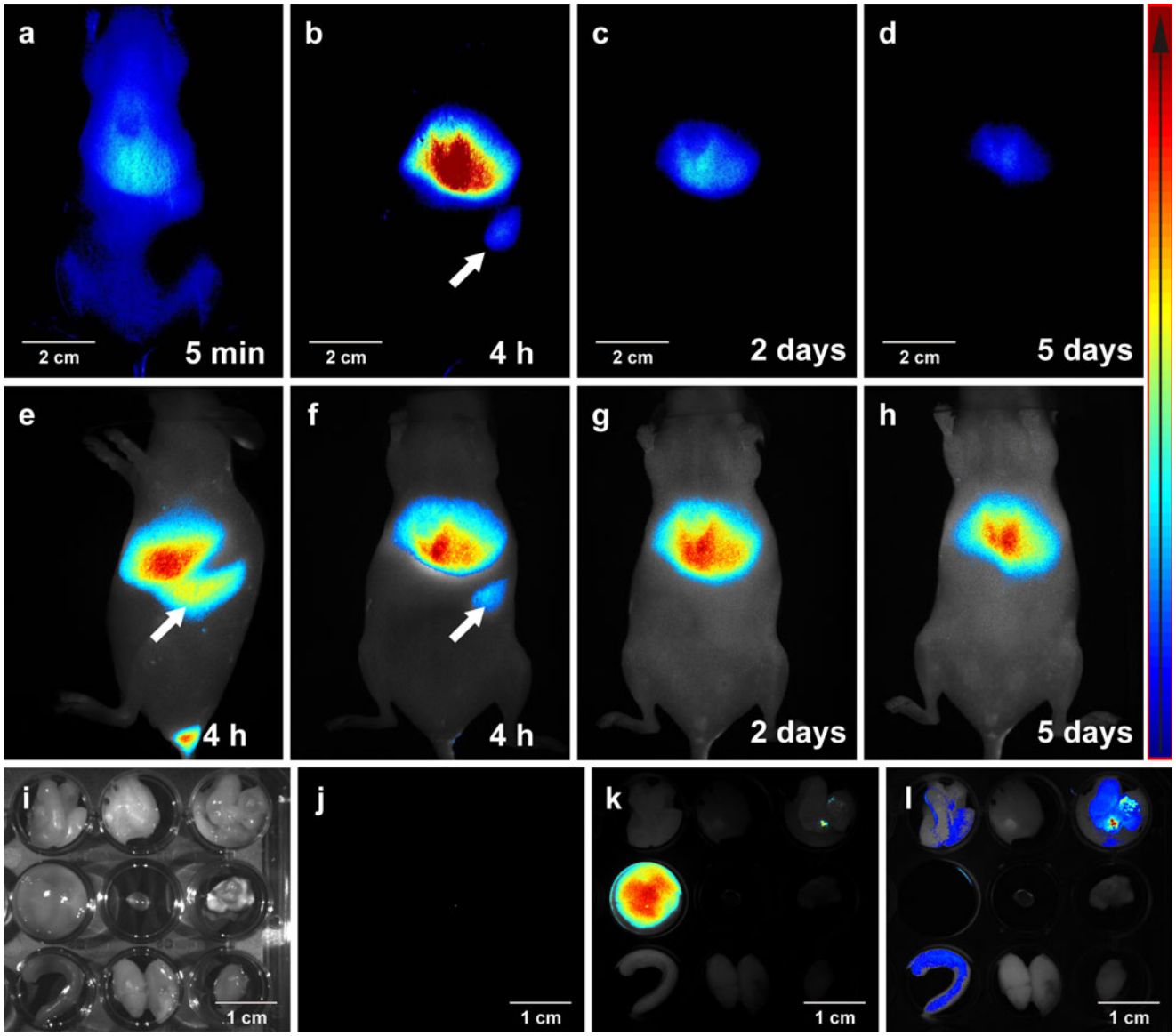

Fig. 4 (**a**–**d**) Comparative fluorescence intensity images of a nude, female mouse as chronological sequence; (**e**–**h**) jet color fluorescence intensity images of the left (**e**) and ventral side (**f**–**h**) of the same nude, female mouse (exposure time = 200 ms); (**i**–**l**) *ex vivo* intensity images of several organs in the following order from left to right, initiating from the top: intestine, fat, uterus with ovary, liver, gall bladder, lung, spleen, kidneys and heart; (**i**) original image; (**j**) untreated mouse and jet color intensity images 24 h after application: (**k**) (exposure time = 400 ms) and (**l**) (2000 ms exposure time and with masked liver).

increased. Nevertheless, the total signal is a value with lower variability between different measurements. The normalized maximum and total intensities from selected organs are shown in Fig. 5. Neither exposure time nor usage of the black plastic plate had an influence on the results (except the liver). Thus, potential errors caused by different exposure times which are not in the optimum range of the respective organ can be excluded, and results obtained by automatically set exposure times can be compared. It is also worth noting that the standard deviation is much larger for the maximum signal (Fig. 5b) compared to total intensity (Fig. 5a).

As shown in Fig. 5a, *ex-vivo* results confirm the nanoparticle accumulation in the RES organs liver and spleen as already detected *in vivo*. No total intensity was noticed in fat tissues and the lungs, and only slight signals were present in the intestines and in the kidneys. Overall, the same trend was found when analysing the normalized maximum intensities (Fig. 5b). Interestingly, a maximum signal of about 25% was also found in the lung. However, a distinct accumulation of the nanoparticles in the lungs appears not to be due to the standard deviation. This was very high and there was neither a signal found in the evaluation of the total signal nor in the images as shown in Fig. 4l. Other

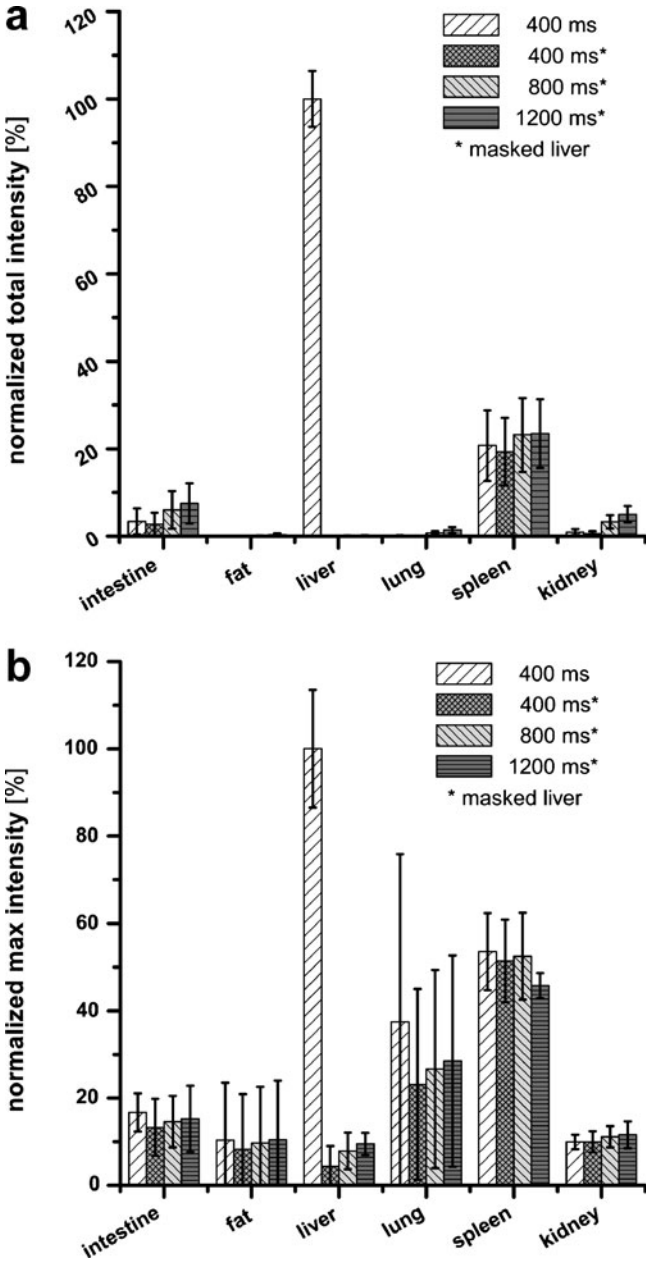

Fig. 5 Exposure time related total (**a**) and maximum (**b**) intensities from different organs measured with different exposure times ($n = 4$).

viscera like fat tissue and kidneys showed maximum intensity levels of 10% or less, which is in the same range of the masked liver values. This can be attributed to the detection limits using the maximum intensity values. Intensities of about 15% were found in the intestine, confirming the image results (Fig. 4l) as well as the calculated total intensity (Fig. 5a). The different fluorescence ratios (liver to spleen) of about 5:1 for the total signal and 2:1 for the maximum are due to differences in the size of the organs. The spleen is much smaller than the liver.

The influence of the nanoparticle concentration on their biodistribution is shown in Fig. 6. These experiments were carried out to evaluate the influence of varying nanoparticle amounts on the accumulation behaviour and to determine the detection limits for imaging. The injection of 60 µL with a nanoparticle concentration of 2.0 mg/mL (injected mass 0.12 mg) did not allow meaningful data analysis due to the too low fluorescence intensity. The range between 4.0 and 6.5 mg/mL (injected mass between 0.24 and 0.39 mg) yielded reproducible results with an average variation of about 15% or less. The total signals were independent of the sex of the mice. However, the age of the mice may be an important factor: Total signals in the spleen were higher in the mice that were three times older (Fig. 6), probably due to the increase in organ size with age. Age dependence was not observed in the liver signal, but this organ is bigger than the hole of the well plate, and only a part of the liver (similar in size for all mice) was studied.

CONCLUSION

This work demonstrates the preparation, characterization and application of PEG-PLA block polymer nanoparticles with defined sizes and narrow size distribution. To prolong the *in vivo* circulation time, PEG with an average molecular weight of 2000 was covalently bound to PLA,

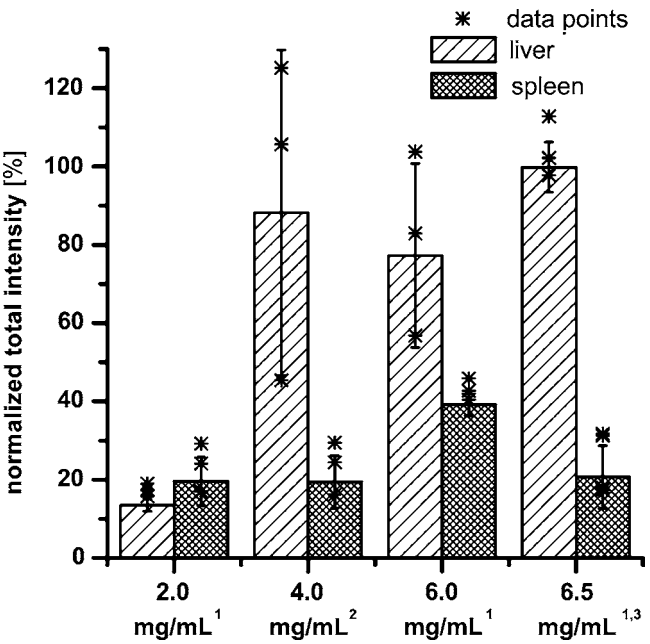

Fig. 6 Normalized total *ex vivo* intensities of different batch D nanoparticle injection concentrations: 2.0, 4.0, 6.0 and 6.5 mg per 1 mL with an age of 3, 3, 9 and 3 months from the left ([1]=female, [2]=male; $n = 3$, [3]$n = 4$).

and nanoparticles composed of PEG-PLA block copolymers could be prepared. Nanoparticles were lyophilized to assure long-term stability, but even the aqueous dispersions were stable over at least three months when stored at 5°C. PEG-PLA nanoparticles were biocompatible and non-toxic to CHO and L929 cells, and detailed particle size characterization by PCS, AF4/MALLS and TEM provided accurate size information. AF4/MALLS results showed that even in batches with rather low polydispersity indices (PCS z-average = 166 nm, PDI = 0.13, batch D), 10% of the nanoparticles were smaller than 48 nm (D10) and the same amount larger than 230 nm (D90). This confirms the need to combine different size measurement techniques for detailed particle size characterization as consumption for size-dependent biodistribution studies and underlines the necessity of preparing and characterizing homogeneous nanoparticles for further *in vivo* experiments.

First, *in vivo* experiments with NR-loaded nanoparticles indicated a fast release of the dye from the particles after injection, resulting in rapid dye elimination from the bloodstream. In contrast, incorporation of the highly hydrophobic DiR allowed direct detection of the nanoparticles in the blood stream for up to 6 h. Consequently, these nanoparticles will have sufficient time to accumulate in tumor tissue due to the EPR effect. Detailed information about nanoparticle accumulation in various organs was obtained by fluorescence imaging and measuring the total and maximum fluorescence signals in the organs *ex vivo*. Based on our results, the combination of these values and the comparison with the *in vivo* imaging data appears to be a promising approach to study nanoparticle accumulation in different organs. Furthermore a new calculation approach was described, which allows the comparison of nanoparticle batches with varying fluorescence intensities. This provides the basis for the determination of the influence of varying particle sizes on the *in vivo* fate. In the future, tumor accumulation should be studied using PEG-PLA nanoparticle batches with different sizes but narrow and well-established size distribution in two tumor models with different shapes and growth rates: the colon carcinoma (Ht29) and the ovarian carcinoma (A2780).

ACKNOWLEDGMENTS

Jörg Teßmar is acknowledged for the discussions during the polymer synthesis and nanoparticle preparation steps. We also thank also Anna Hezinger for the help with the TEM measurements and Martina Hennicke and Constanze Gottschalk for taking care of the animals. Parts of the studies were supported by grants from the Federal State of Saxony Anhalt (FKZ 3646A/0907).

REFERENCES

1. Brigger I, Dubernet C, Couvreur P. Nanoparticles in cancer therapy and diagnosis. Adv Drug Deliv Rev. 2002;54:631–51.
2. Peer D, Karp JM, Hong S, FaroKHzad OC, Margalit R, Langer R. Nanocarriers as an emerging platform for cancer therapy. Nature Nanotech. 2007;2:751–60.
3. Maeda H. Tumor-selective delivery of macromolecular drugs via the EPR effect: background and future prospects. Bioconjugate Chem. 2010;21:797–802.
4. Yuan F, Dellian M, Fukumura D, Leunig M, Berk DA, Torchilin VP, *et al.* Vascular-permeability in a human tumor xenograft - molecular-size dependence and cutoff size. Cancer Res. 1995;55:3752–6.
5. Hobbs SK, Monsky WL, Yuan F, Roberts WG, Griffith L, Torchilin VP, *et al.* Regulation of transport pathways in tumor vessels: role of tumor type and microenvironment. Proc Natl Acad Sci USA. 1998;95:4607–12.
6. Moghimi SM, Porter CJH, Muir IS, Illum L, Davis SS. Non-phagocytic uptake of intravenously injected microspheres in rat spleen - influence of particle-size and hydrophilic coating. Biochem Biophys Res Commun. 1991;177:861–6.
7. Moghimi SM, Hunter AC, Murray JC. Long-circulating and target-specific nanoparticles: theory to practice. Pharmacol Rev. 2001;53:283–318.
8. Nakaoka R, Tabata Y, Yamaoka T, Ikada Y. Prolongation of the serum half-life period of superoxide dismutase by poly(ethylene glycol) modification. J Controlled Release. 1997;46:253–61.
9. Litzinger DC, Buiting AMJ, Vanrooijen N, Huang L. Effect of liposome size on the circulation time and intraorgan distribution of amphipathic Poly(Ethylene Glycol)-Containing Liposomes. Biochim Biophys Acta, Biomembr. 1994;1190:99–107.
10. Liu DX, Mori A, Huang L. Role of liposome size and res blockade in controlling biodistribution and tumor uptake of Gm1-containing liposomes. Biochim Biophys Acta. 1992;1104:95–101.
11. Storm G, Belliot SO, Daemen T, Lasic DD. Surface modification of nanoparticles to oppose uptake by the mononuclear phagocyte system. Adv Drug Deliv Rev. 1995;17:31–48.
12. Gaumet M, Vargas A, Gurny R, Delie F. Nanoparticles for drug delivery: the need for precision in reporting particle size parameters. Eur J Pharm Biopharm. 2008;69:1–9.
13. Dunn SE, Coombes AGA, Garnett MC, Davis SS, Davies MC, Illum L. *In vitro* cell interaction and *in vivo* biodistribution of poly (lactide-co-glycolide) nanospheres surface modified by poloxamer and poloxamine copolymers. J Controlled Release. 1997;44:65–76.
14. Kwon GS, Kataoka K. Block-copolymer micelles as long-circulating drug vehicles. Adv Drug Deliv Rev. 1995;16:295–309.
15. Hezinger AFE, Tessmar J, Gopferich A. Polymer coating of quantum dots—A powerful tool toward diagnostics and sensorics. Eur J Pharm Biopharm. 2008;68:138–52.
16. Medintz IL, Uyeda HT, Goldman ER, Mattoussi H. Quantum dot bioconjugates for imaging, labelling and sensing. Nature Mater. 2005;4:435–46.
17. Smith AM, Duan HW, Mohs AM, Nie SM. Bioconjugated quantum dots for *in vivo* molecular and cellular imaging. Adv Drug Deliv Rev. 2008;60:1226–40.
18. Frangioni JV. *In vivo* near-infrared fluorescence imaging. Curr Opin Chem Biol. 2003;7:626–34.
19. Derfus AM, Chan WCW, Bhatia SN. Probing the cytotoxicity of semiconductor quantum dots. Nano Lett. 2004;4:11–8.
20. Lucke A, Tessmar J, Schnell E, Schmeer G, Gopferich A. Biodegradable poly(D, L-lactic acid)-poly(ethylene glycol)-monomethyl ether diblock copolymers: structures and surface properties relevant to their use as biomaterials. Biomaterials. 2000;21:2361–70.

21. Fessi H, Puisieux F, Devissaguet JP, Ammoury N, Benita S. Nanocapsule formation by interfacial polymer deposition following solvent displacement. Int J Pharm. 1989;55:R1–4.
22. Rose C. Particulate systems for Fluorescence Imaging and Drug Delivery. Thesis: University of Regensburg; 2010.
23. Kuntsche J, Klaus K, Steiniger F. Size determinations of colloidal fat emulsions: a comparative study. J Biomed Nanotechnol. 2009;5:384–95.
24. Westedt U, Kalinowski M, Wittmar M, Merdan T, Unger F, Fuchs J, *et al.* Poly(vinyl alcohol)-graft-poly(lactide-co-glycolide) nanoparticles for local delivery of paclitaxel for restenosis treatment. J Controlled Release. 2007;119:41–51.
25. Mosmann T. Rapid colorimetric assay for cellular growth and survival—Application to proliferation and cyto-toxicity assays. J Immunol Methods. 1983;65:55–63.
26. Schaffer BS, Grayson MH, Wortham JM, Kubicek CB, McCleish AT, Prajapati SI, *et al.* Immune competency of a hairless mouse strain for improved preclinical studies in genetically engineered mice. Mol Cancer Ther. 2010;9:2354–64.
27. Leblond F, Davis SC, Valdes PA, Pogue BW. Pre-clinical whole-body fluorescence imaging: review of instruments, methods and applications. J Photoch Photobio B. 2010;98:77–94.
28. Mansfield JR, Gossage KW, Hoyt CC, Levenson RM. Autofluorescence removal, multiplexing, and automated analysis methods for *in-vivo* fluorescence imaging. J Biomed Opt. 2005;10.
29. Zimmermann T, Rietdorf J, Pepperkok R. Spectral imaging and its applications in live cell microscopy. FEBS Lett. 2003;546:87–92.
30. Cheng FY, Wang SPH, Su CH, Tsai TL, Wu PC, Shieh DB, *et al.* Stabilizer-free poly(lactide-co-glycolide) nanoparticles for multimodal biomedical probes. Biomaterials. 2008;29:2104–12.
31. Putaux JL, Buleon A, Borsali R, Chanzy H. Ultrastructural aspects of phytoglycogen from cryo-transmission electron microscopy and quasi-elastic light scattering data. Int J Biol Macromol. 1999;26:145–50.
32. Lohrke J, Briel A, Mader K. Characterization of superparamagnetic iron oxide nanoparticles by asymmetrical flow-field-flow-fractionation. Nanomedicine. 2008;3:437–52.
33. Stauch O, Schubert R, Savin G, Burchard W. Structure of artificial cytoskeleton containing liposomes in aqueous solution studied by static and dynamic light scattering. Biomacromolecules. 2002;3:565–78.
34. Coffin MD, Mcginity JW. Biodegradable pseudolatexes—the chemical-stability of Poly(D, L-Lactide) and poly (Epsilon-Caprolactone) nanoparticles in aqueous-media. Pharm Res. 1992;9:200–5.
35. Dunne M, Corrigan OI, Ramtoola Z. Influence of particle size and dissolution conditions on the degradation properties of polylactide-co-glycolide particles. Biomaterials. 2000;21:1659–68.
36. Lin WJ, Chen YC, Lin CC, Chen CF, Chen JW. Characterization of pegylated copolymeric micelles and *in vivo* pharmacokinetics and biodistribution studies. J Biomed Mater Res Part B. 2006;77B:188–94.
37. Honig MG, Hume RI. Fluorescent carbocyanine dyes allow living neurons of identified origin to be studied in long-term cultures. J Cell Biol. 1986;103:171–87.
38. Texier I, Goutayer M, Da Silva A, Guyon L, Djaker N, Josserand V, et al. Cyanine-loaded lipid nanoparticles for improved *in vivo* fluorescence imaging. J Biomed Opt. 2009;14.
39. Chen J, Corbin IR, Li H, Cao WG, Glickson JD, Zheng G. Ligand conjugated low-density lipoprotein nanoparticles for enhanced optical cancer imaging *in vivo*. J Am Chem Soc. 2007;129:5798.
40. Kuffler DP. Long-term survival and sprouting in culture by motoneurons isolated from the spinal-cord of adult frogs. J Comp Neurol. 1990;302:729–38.
41. Weissleder R. A clearer vision for *in vivo* imaging. Nat Biotechnol. 2001;19:316–7.
42. Hardin J. Confocal and multi-photon imaging of living embryos. In Pawley JB, Masters BR, editors. Handbook of biological confocal microscopy. J Biomed Opt. 2008;760.
43. Jores K, Haberland A, Wartewig S, Mader K, Mehnert W. Solid lipid nanoparticles (SLN) and oil-loaded SLN studied by spectrofluorometry and raman spectroscopy. Pharm Res. 2005;22:1887–97.
44. Petersen S, Fahr A, Bunjes H. Flow cytometry as a new approach to investigate drug transfer between lipid particles. Mol Pharmaceutics. 2010;7:350–63.
45. N.n. Public Chemical Database. Public Chemical Database. 2010.
46. Greenspan P, Mayer EP, Fowler SD. Nile red—A selective fluorescent stain for intracellular lipid droplets. J Cell Biol. 1985;100:965–73.
47. Rashid F, Horobin RW, Williams MA. Predicting the behaviour and selectivity of fluorescent probes for lysosomes and related structures by means of structure-activity models. Histochem J. 1991;23:450–9.
48. Rashid F, Horobin RW. Interaction of molecular probes with living cells and tissues.2. A structure-activity analysis of mitochondrial staining by cationic probes, and a discussion of the synergistic nature of image-based and biochemical approaches. Histochem Cell Biol. 1990;94:303–8.
49. Ivanov AI, Gavrilov VB, Furmanchuk DA, Aleinikova O, Konev SV, Kaler GV. Fluorescent probing of the ligand-binding ability of blood plasma in the acute-phase response. Clin Exp Med. 2002;2:147–55.
50. Gordon S, Tee RD, Taylor AJN. Analysis of rat urine proteins and allergens by sodium Dodecyl-Sulfate Polyacrylamide-Gel electrophoresis and immunoblotting. J Allergy Clin Immun. 1993;92:298–305.
51. Lim HJ, Parr MJ, Masin D, McIntosh NL, Madden TD, Zhang GY, *et al.* Kupffer cells do not play a role in governing the efficacy of liposomal mitoxantrone used to treat a tumor model designed to assess drug delivery to liver. Clin Cancer Res. 2000;6:4449–60.
52. Bazile D, Prudhomme C, Bassoullet MT, Marlard M, Spenlehauer G, Veillard M. Stealth Me.Peg-Pla nanoparticles avoid uptake by the mononuclear phagocytes system. J Pharm Sci. 1995;84:493–8.
53. Verrecchia T, Spenlehauer G, Bazile DV, Murrybrelier A, Archimbaud Y, Veillard M. Non-stealth (Poly(Lactic Acid Albumin)) and stealth (Poly(Lactic Acid-Polyethylene Glycol)) nanoparticles as injectable drug carriers. J Controlled Release. 1995;36:49–61.
54. Gref R, Miralles G, Dellacherie E. Polyoxyethylene-coated nanospheres: effect of coating on zeta potential and phagocytosis. Polym Int. 1999;48:251–6.